ELSEVIER

PII: S0309-1708(98)00013-X

Advances in Water Resources Vol. 22, No. 3, pp. 203–221, 1998
© 1998 Elsevier Science Ltd
Printed in Great Britain. All rights reserved
0309-1708/98/$ - see front matter

Analysis of subsurface contaminant migration and remediation using high performance computing

Andrew F. B. Tompson[a,*], Robert D. Falgout[b], Steven G. Smith[b], William J. Bosl[b] & Steven F. Ashby[b]

[a]*Geosciences and Environmental Technologies Division, Lawrence Livermore National Laboratory, Livermore, CA 94550, USA*
[b]*Center for Applied Scientific Computation, Lawrence Livermore National Laboratory, Livermore, CA 94550, USA*

Highly resolved simulations of groundwater flow, chemical migration and contaminant recovery processes are used to test the applicability of stochastic models of flow and transport in a typical field setting. A simulation domain encompassing a portion of the upper saturated aquifer materials beneath the Lawrence Livermore National Laboratory was developed to hierarchically represent known hydrostratigraphic units and more detailed stochastic representations of geologic heterogeneity within them. Within each unit, Gaussian random field models were used to represent hydraulic conductivity variation, as parameterized from well test data and geologic interpretation of spatial variability. Groundwater flow, transport and remedial extraction of two hypothetical contaminants were made in six different statistical realizations of the system. The effective flow and transport behavior observed in the simulations compared reasonably with the predictions of stochastic theories based upon the Gaussian models, even though more exacting comparisons were prevented by inherent nonidealities of the geologic model and flow system. More importantly, however, biases and limitations in the hydraulic data appear to have reduced the applicability of the Gaussian representations and clouded the utility of the simulations and effective behavior based upon them. This suggests a need for better and unbiased methods for delineating the spatial distribution and structure of geologic materials and hydraulic properties in field systems. High performance computing can be of critical importance in these endeavors, especially with respect to resolving transport processes within highly variable media. © 1998 Elsevier Science Limited. All rights reserved

Keywords: contaminant transport, porous media, remediation, heterogeneity, high performance computation.

1 INTRODUCTION

It is well known that subsurface formations are spatially heterogeneous in their structure and material composition, as well as their hydraulic and chemical properties. These conditions create nonuniform groundwater flow fields and strongly influence the migration of dissolved chemicals and contaminants through accelerated dispersion, dilution and retardation processes.[8,12,29] In subsurface pollution problems, contaminants are usually found to be distributed in distinct, three-dimensional patterns, as influenced by flow in more conductive lenses and strata, diffusion into less permeable zones, sorption onto variably reactive minerals, and a sporadic history of introduction into the subsurface.

*Corresponding author.

In this paper, we are interested in the use of numerical models to stimulate flow of groundwater and reactive transport of contaminants in the subsurface. We are particularly concerned with how the effects of heterogeneity can be appropriately incorporated and represented within models used in actual field problems. As a result, we plan to use a case study to test the applicability of effective-medium stochastic theories of flow and transport in a typical field setting. These theories are generally meant to provide a more defensible framework to predict mean rates of flow and dispersion behavior in nonuniform geologic formations from a bulk, homogenized perspective.[8,12]

To do this, we will employ a simple model of geologic heterogeneity to support the parameterization of these theories at the application site. Our approach will rely on the development of a Gaussian geostatistical representation

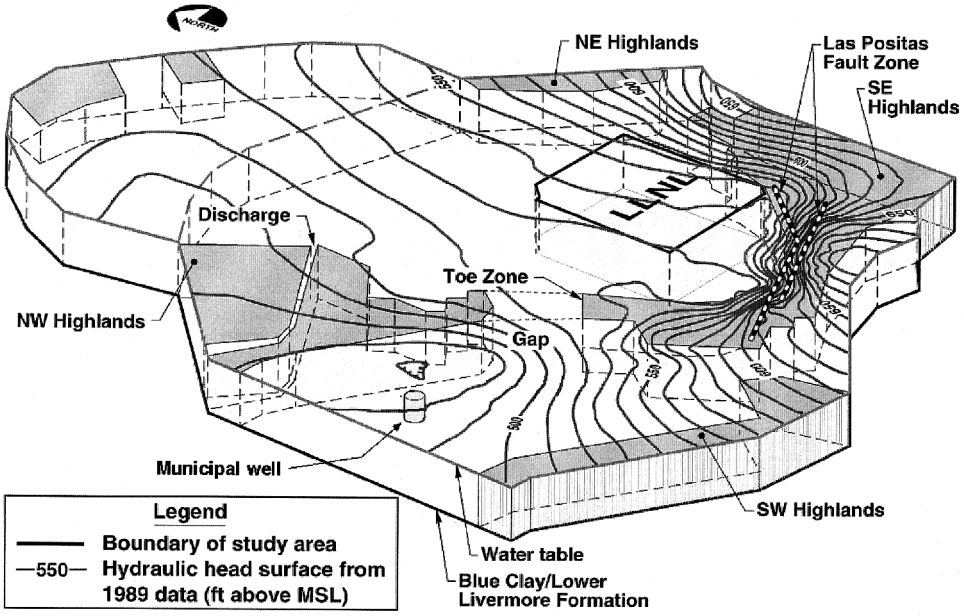

Fig. 1. Perspective conceptualization (looking northeast) of the upper aquifer beneath LLNL, showing alluvial materials (white), less permeable uplifted zones (dark), and a downtown pumping well. Approximate, vertically averaged hydraulic head contours are also shown. The lower boundary of the aquifer overlays a relatively consistent, impermeable blue clay formation throughout the region. Flow in the alluvium goes mainly from the east and southeast toward the west.

of conductivity variability using available geologic and hydraulic test data. This will be accomplished hierarchically within a series of previously identified hydrostratigraphic units that comprise the saturated geologic system at the site. Because these units are bounded, highly variable and potentially nonstationary, we will use a more detailed, experimental modeling framework for the selective validation of the stochastic results, as opposed to relying on sparse observational data for the same purpose.

Thus, a series of flow and point-source transport simulations will be carried out in the manner of Tompson and Gelhar[26] in several equally likely, detailed ''realizations'' of the system that have been built from the same hydrostratigraphic and Gaussian random field conceptualization. Effective flow and dispersive transport characteristics will be identified and compared with theoretical predictions. Importantly, this work will also examine limitations of this procedure that relate to biases and shortcomings in the available data, idealizations in the geostatistical and stochastic models, and the overall value of the effective-medium problem conceptualization.

2 EXAMPLE FIELD APPLICATION

Our example application is centered on the flow and contaminant migration processes in the upper aquifer materials beneath the Lawrence Livermore National Laboratory (LLNL) in California. The groundwater in this area was contaminated with some eight volatile organic compounds (VOCs) that were in regular use 50 years ago when the lab site was occupied by a naval airfield. The existing saturated zone contamination is comprised chiefly of trichloroethlyene (TCE) and perchloroethylene (PCE). This contamination extends from beneath LLNL to over a mile west, is slowly moving toward municipal wells in downtown Livermore, and is the focus of a large pump-and-treat remediation project.[23]

Detailed measurements of contaminant migration rates are limited or unavailable, partially because the observational framework is coarse and largely less than 10 years old, and partially because it is difficult to pinpoint specific, self-contained plumes. The current contamination has been derived from multiple source events that occurred over a wide period of time.

The upper aquifer beneath LLNL is composed of widespread alluvial materials as deposited and built up from meandering streams that cross the Livermore Valley. It lies above a rather continuous, blue–green clay layer that is considered to be the top of the so-called Lower Livermore Formation. In addition, there are several other less-permeable zones close to LLNL, associated with surrounding highlands, as well as a nearby uplifted fault zone. A schematic of this area is shown in Fig. 1.

The alluvial materials have been further classified in terms of four principal geologic facies.[5,11] These include widespread low-permeability floodplain deposits containing mostly clays and silts, moderate-permeability levee deposits containing silts and sands, moderate-permeability debris flows containing a wide mixture of clays, silts, sands and gravels, and higher-permeability channel materials composed mostly of sands and gravels.

A two-dimensional, vertically integrated, regional modeling study of flow and transport in the LLNL system has

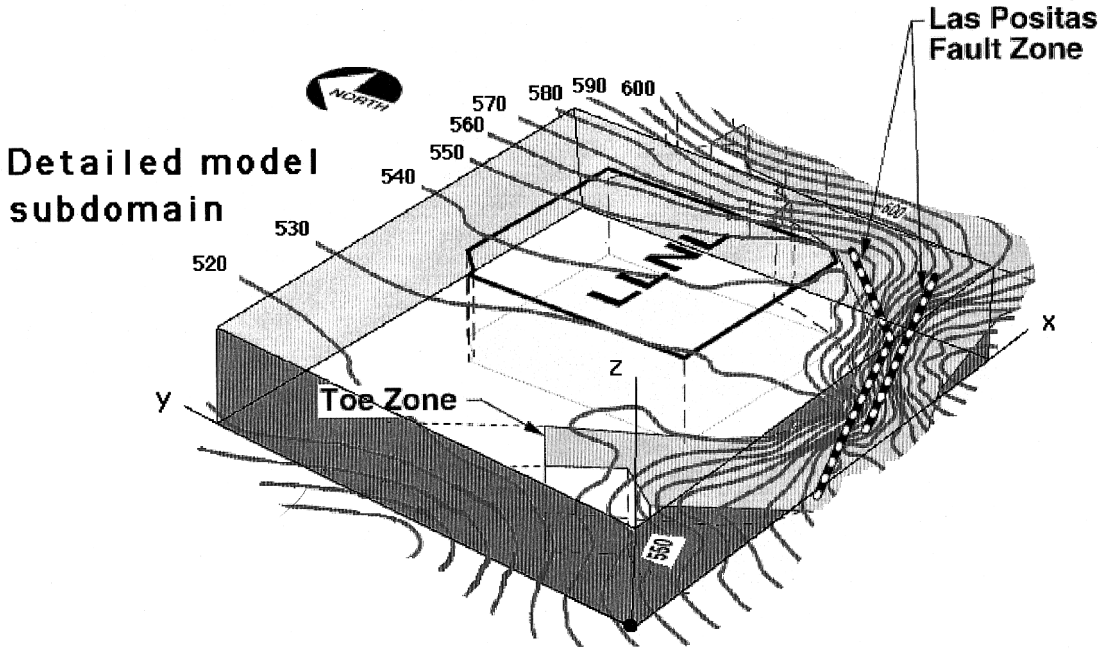

Fig. 2. Perspective conceptualization (looking northeast) of the detailed modeling domain around LLNL (refer to Fig. 1). Approximate, vertically averaged hydraulic head contours shown at 10 ft intervals.

been carried out, under both natural and remedial conditions.[28] This has been based on a simplified representation of the flow and transport processes in the alluvial materials above the blue–green clay, a number of physical and chemical property measurements taken from over 400 wells at the site and a reasonable amount of geologic interpretation to conceptualize the hydrologic system and approximate the contaminant distribution.[25] The regional model simulation domain is shown in Fig. 1.

2.1 Modeling subdomain

In the current application, attention will be focused on a smaller subdomain comprised of a 12 700 ft square prismatic block of alluvium ''carved'' out of the upper 320 ft of saturated aquifer surrounding the LLNL site (Fig. 2). Hydraulic conditions in the block will be considered to be approximately confined, with the upper portion located close to the water table. The lower portion of the block (at elevation 230 ft) intersects much of the bounding blue–green clay formation, while its southeast corner is crossed by the fault zone. This block envelopes all of the currently contaminated groundwater.

Material properties such as the hydraulic conductivity, medium porosity or mineral sorptive capacity will be specified separately for the alluvial materials, the clay layer and the uplifted fault zone. In addition, the alluvial materials will be divided into eight recently identified hydrostratigraphic layers,[4] as shown in Fig. 3. These layers have been identified from geologic cross-sections constructed from well logs, core descriptions and hydraulic interference tests.

Fig. 4 shows the locations of approximately 240 monitoring wells within the modeling subdomain from which measurements of hydraulic conductivity are available from well tests. The different symbols correspond to the principal hydrostratigraphic interval in which the wells were screened. Most well screens were between 5 and 15 ft in length and were situated in primarily high- to moderate-permeability materials. This was done in anticipation of the wells being used for monitoring and remediation purposes. As shown in Fig. 5a, there was a significant degree of variability and spread in the conductivity measurements, despite the fact that lower-permeability materials were not effectively incorporated and accounted for in the testing procedure.

Fig. 5a also shows a normalized histogram of 46 conductivity measurements made in a series of three-inch saturated-zone soil cores. The cores were obtained during the construction of three wells located near the southwest corner of the LLNL site (Fig. 4). These data are more reflective of the lower-permeability materials from which intact cores could be taken, and do not effectively represent higher permeability sandy or gravelly materials that could not be retained in the cores. Despite the disparity in testing scales and the fact that both histograms represent differently biased data sets, the pair of histograms, in combination, do seem to give a clearer indication of the true distribution of conductivity in the alluvial materials.

At this stage, it would appear that additional conductivity measurements or lithological analyses would be required to provide a more unbiased and unified picture of the alluvial conductivity distribution. Nevertheless, in what follows, we will use the more abundant well test measurements as the principal means to describe the physical heterogeneity of the system. These will be used in a provisional fashion

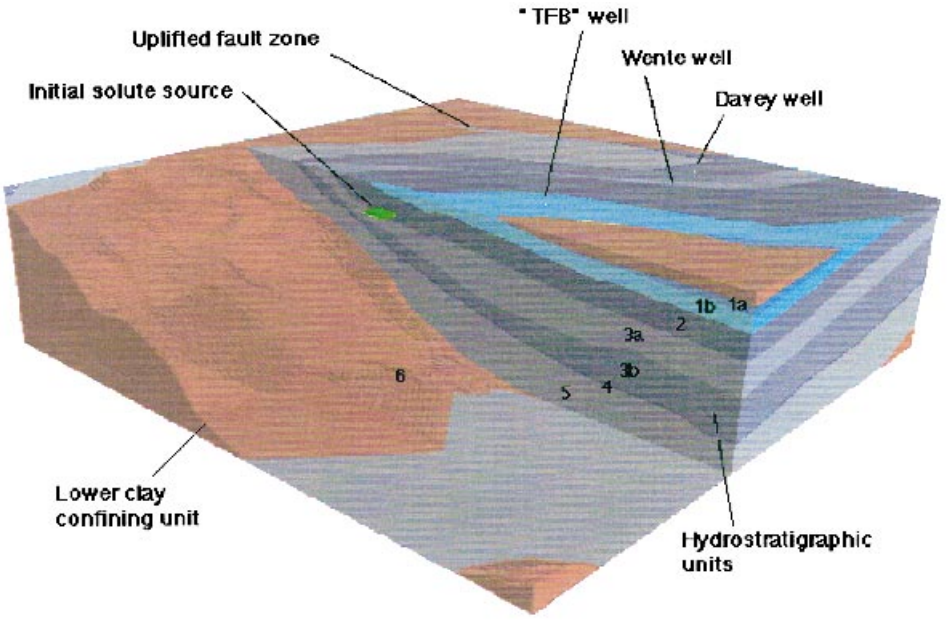

Fig. 3. Perspective of the model subdomain (looking southeast), showing the principal hydrostratigraphic units (1–5) lying above a lower confining clay unit (6). Vertical scale exaggerated by a factor of 10. Locations of the Wente and Davey agricultural wells and the Treatment facility ''B'' (TFB) extraction well are also shown, as is the uplifted fault zone. Initial source location used in transport experiments shown in green. In the electronic version of this paper, two animated sequences are available to help visualize the hydrostratigraphic units more clearly (see ''Special section on Visualization'' on the journal's homepage at **http://www.elsevier.nl/locate/advwatres** or **http:www.elsevier.com/locate/advwatres**).

only, with the caveat that more effective or complete descriptions of the conductivity distribution can be substituted as they become available.

3 SIMULATION APPROACH

Detailed simulations of flow and transport in the subdomain will be made in a number of equally-probable ''realizations'' of the system that preserve the structure and geometry of the hydrostratigraphic layers and recreate, in an approximate statistical sense, the characteristic degree of property variability that has been observed in each of them. Fig. 5b shows that variability in the hydraulic conductivity exists throughout each hydrostratigraphic layer as well. In addition, the uplifted fault zone will be retained as ''fixed'' features with constant properties in each realization. In this sense, the spacing and arrangement of the measurement points will not influence the character of heterogeneity produced in any given realization.

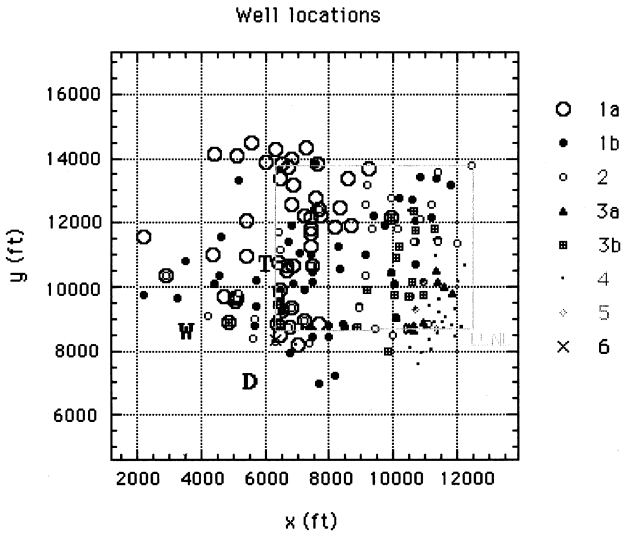

Fig. 4. The 240 well locations in the model subdomain where hydraulic conductivities were measured. Symbols indicate hydrostratigraphic layer in which each well was screened. LLNL site outlined in light gray color. ''D'', ''W'' and ''T'' refer to the locations of the Davey, Wente and TFB wells used in the simulations.

3.1 Flow and transport processes

Steady, saturated flow in this system is described by

$$\nabla\cdot(K\nabla h) = \sum_w Q_w \delta(\mathbf{x} - \mathbf{x}_w) \tag{1}$$

where $h(\mathbf{x})$ is the hydraulic head [L], $K(\mathbf{x})$ is the medium hydraulic conductivity [L/T], and $Q_w > 0$ [L^3/T] represents a loss of fluid due to extraction pumping at location x_w. Use of fixed Dirichlet boundary conditions for h will allow for fluid inflow across the boundaries to balance losses from pumping.

The average groundwater seepage velocity, $\mathbf{v}(\mathbf{x})$ [L/T], is defined by

$$\epsilon\mathbf{v} = -K\nabla h \tag{2}$$

where ϵ is the medium porosity.

The migration of a dissolved, neutrally buoyant chemical

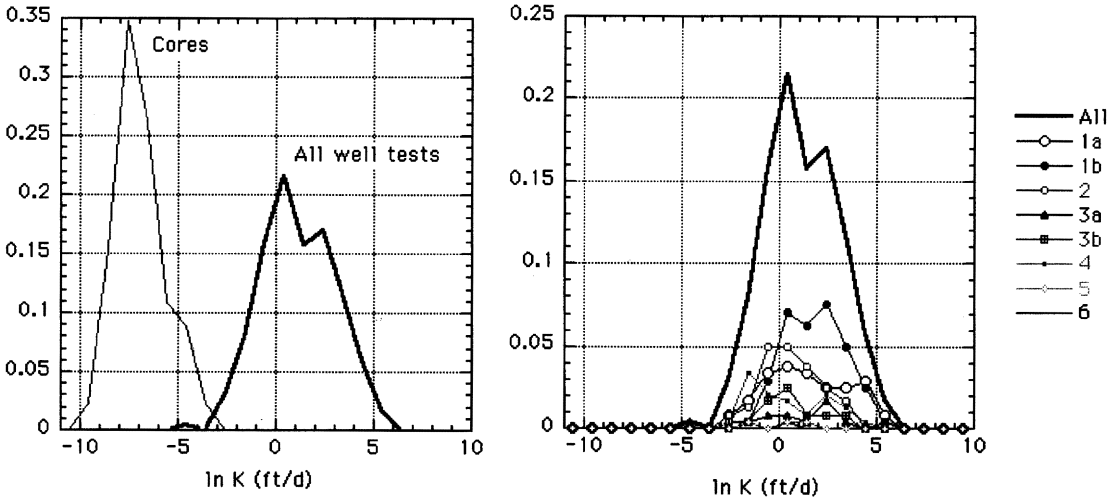

Fig. 5. (a) Normalized histogram of hydraulic conductivity measurements made from 240 well and 46 core tests. (b) Well conductivity histogram replotted with respect to hydrostratigraphic layer. Symbols in (b) correspond to layers and symbols in Table 1 and Fig. 4.

constituent in the groundwater is described by

$$\frac{\partial(\mathcal{R}\epsilon c)}{\partial t} + \nabla\cdot(\epsilon c\mathbf{v}) - \nabla\cdot(\epsilon\mathbf{D}\cdot\nabla c) = -c\sum_w Q_w\delta(\mathbf{x}-\mathbf{x}_w) \tag{3}$$

where $c(\mathbf{x},t)$ is the average aqueous concentration [M/L^3] at a point in the medium.[8] The quantity

$$\mathbf{D}(\mathbf{x}) \approx (\alpha_T|\mathbf{v}| + \mathcal{D})\mathbf{I} + (\alpha_L - \alpha_T)\frac{\mathbf{vv}}{|\mathbf{v}|} \tag{4}$$

is the velocity-dependent hydrodynamic dispersion tensor [L^2/T], α_L and α_T are the local longitudinal and transverse dispersivities [L], and $\mathcal{D}$ is the aqueous molecular diffusivity [L^2/T]. In eqn (3) we have assumed that sorption onto the mineral phase may occur reversibly and in an equilibrium fashion such that the total (aqueous plus sorbed) concentration may be related to the aqueous concentration by $\rho(\mathbf{x},t) = \epsilon c + (1-\epsilon)s = \epsilon cR$, where, $s(\mathbf{x},t)$ is the sorbed mass per unit volume of soil matrix (concentration) [M/L^3] and $\mathcal{R}$ is the local partitioning or retardation capacity of the soil, which may generally be concentration dependent.

In the experiments below, we consider both a nonreactive tracer (where $\mathcal{R}_{\text{tracer}} = 1$) and a reactive compound such as perchloroethylene (PCE) that is present at the LLNL site.[23] We assume that PCE will linearly sorb onto the soil matrix such that $\mathcal{R}_{\text{PCE}} = 1 + \epsilon k_d/(1-\epsilon)$, where k_d is a dimensionless sorption coefficient.

3.2 Specification of material properties

In the alluvium, heterogeneity in the hydraulic conductivity (K) will be specified in terms of a simple and approximate Gaussian random field model.[8,12,24] In each hydrostratigraphic layer, the spatial distribution of K is assumed to be described by

$$\ln K_j(\mathbf{x}) \approx F_j + f_j(\mathbf{x}) \tag{5}$$

where F_j is the mean of the ln K distribution in layer j and $f_j(\mathbf{x})$ is a spatially fluctuating component with standard deviation σ_{fj}. Values of F_j (or, more conveniently, the geometric mean conductivity, $K_{Gj} = e^{F_j}$) and σ_{fj} for each layer j can be inferred from distributional data such as that in Fig. 5b.

Spatial persistence in values of $K(\mathbf{x})$ is prescribed by a model of spatial correlation for $f_j(\mathbf{x})$ in each unit. Here, we have used an anisotropic exponential correlation model of the form

$$C_j(\mathbf{r}) = \sigma_{fj}^2 \exp\left\{-\left[(r_1/\lambda_{j1})^2 + (r_2/\lambda_{j2})^2 + (r_3/\lambda_{j3})^2\right]^{1/2}\right\} \tag{6}$$

where $\mathbf{r}$ is a separation, or lag vector, and λ_{ji} is a correlation length scale for direction i in Unit j.

Although this model is quite common,[8,12] it should still be regarded as approximate because of limitations in the hard data needed to implement it and its overall conceptual simplicity. More sophisticated and geologically realistic methods based upon non-Gaussian random fields,[17] indicator simulation[14,10,15,5,6] or alluvial deposition models[30,31] could also be used to specify formation heterogeneity.

Preliminary analyses of the well test data in Fig. 5 have allowed the statistical properties shown in Table 1 to be estimated for the LLNL subdomain. As mentioned previously, these will be used with some reservations, owing to the high bias inherent in the well test data. Nevertheless, the trends in the geometric mean conductivities and ln K standard deviations are consistent with general observations that indicate, for example, that Units 1b and 4 are generally more uniform in content and composed of permeable sands, while Units 3a and 3b are more heterogeneous with broader mixtures of clay, silt and sand.

Correlation lengths are notoriously difficult to determine, especially when closely spaced data are few in number. Fig. 6 shows several horizontal variograms estimated from the Unit 1b data. They seem to indicate that some horizontal anisotropy may be present in which the correlation lengths

Table 1. Statistical characteristics used to specify hydraulic conductivity heterogeneity within each hydrostratigraphic unit using the random field model (eqns (5) and (6)). Effective horizontal hydraulic conductivity values predicted from eqn (8) are also shown

Unit, j	$K_{Gj} = e^{F_j}$ (ft/day)	σ_{fj}	Specified $\lambda_x = \lambda_y$ (ft)	λ_z (ft)	Predicted $\hat{K}_{hj}/K_{Gj}$
1a	4.6	2.1	200	10	3.04
1b	5.9	1.6	200	10	2.19
2	2.0	1.4	200	10	1.91
3a	1.5	2.3	200	10	3.44
3b	1.9	2.3	200	10	3.44
4	2.6	1.5	200	10	2.04
5	1.4	2.0	200	10	2.85
6 (clay)	0.1	1.0	200	10	1.91
Fault zone	0.004	0.0	—	—	1.0
1a–5	3.3	1.8	200	10	2.5

lie between 100 and 250 ft. For the purposes of this investigation, we will assume that correlation is approximately isotropic in the horizontal plane with a length scale of 200 ft. Additional analyses of data in units 1a and 2–5 suggest that the same correlation approximation may be used. Vertical correlation scales shown in Table 1 have been estimated from some vertical variograms and borehole geophysical analyses.

In the lower clay zone (Unit 6), the conductivity distribution is also assumed to be heterogeneous, albeit with a very small mean, K_G, consistent with approximately confining conditions. In the uplifted fault materials, K will be assigned a constant value of 0.004 ft/day with no spatial variability. This is consistent with earlier interpretations used in Ref. [28].

A single realization of the hydraulic conductivity distribution in the local subdomain is shown in Fig. 7. An unconditional Turning Bands technique[24] was used to generate independent data fields within each layer. By unconditional, we mean that specific values of K that may actually be known at specific locations were not necessarily reproduced in the simulation. This is an important limitation that will be addressed in future work. In addition, the principal horizontal correlation axes of the random field in each layer were allowed to drape over or conform to the curvature of the most immediate lower hydrostratigraphic unit boundary, as a means to approximate a slight depositional dip or strike in the field.

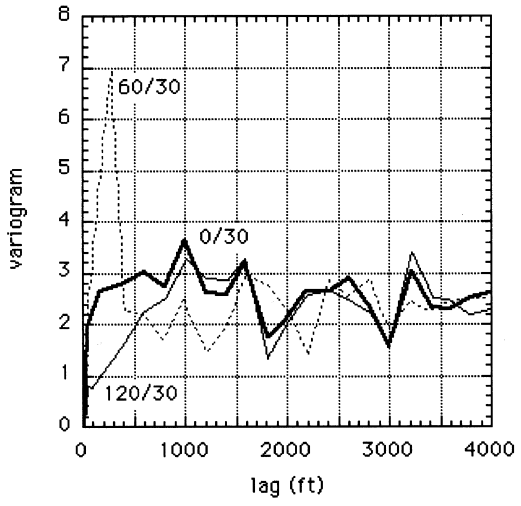

Fig. 6. Estimated horizontal variograms for hydrostratigraphic unit 1b. Each curve incorporates data in 30° arc segments centered on 0° (due North), 60° (East–Southeast), and 120° (West–Southwest).

Based upon preliminary PCE sorption data at LLNL,[3,27] we will assume that the PCE sorptivity of the soil is perfectly correlated with the hydraulic conductivity via

$$\ln(\epsilon k_d) \approx -0.86 - 0.32 \ln K \tag{7}$$

This relationship attempts to relate variabilities in both k_d and K to more fundamental variations in the average specific soil surface areas.[22]

The quantities ϵ, α_L and α_T will be held constant in all cases and set to representative local values of 0.3, 1.0 ft and 0.1 ft, respectively.

3.3 Computational issues

To maintain a spatial resolution that is four times finer than the correlation scale in each coordinate direction, properties were generated on a uniform $257 \times 257 \times 129$ orthogonal grid for all simulations considered. This resulted in a simulation mesh with over 8 million nodes, each separated by grid lengths Δx_i equal to 50, 50 and 2.5 ft, respectively, in each coordinate direction i. In the current work, a standard 7-point finite volume procedure was employed to solve the flow problem (eqn (1)) for the distribution of hydraulic head, from which velocity fields were subsequently calculated using a standard differencing technique.

Because of the size of the subdomain problem and the need for multiple simulations, we employed the newly-developed ParFlow simulator to solve all flow problems of interest.[1,2] ParFlow has been developed for use on a variety of computational platforms, ranging from large-scale, massively parallel computers such as the Cray T3D, where all flow simulations reported here were performed, to

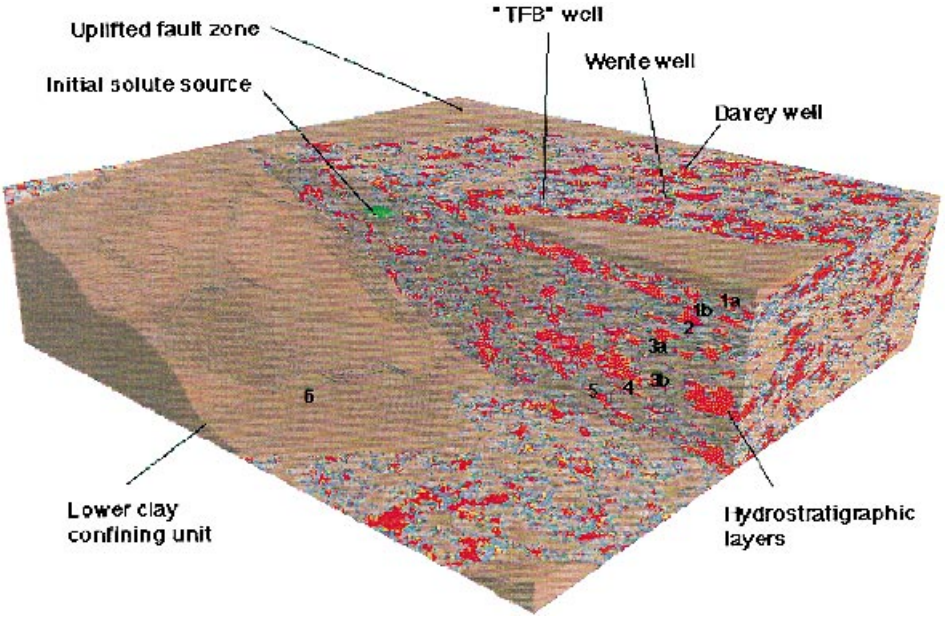

Fig. 7. Perspective of the detailed model subdomain (looking southeast), showing a realization of nonuniform flow properties in the more permeable hydrostratigraphic units (1–5). The lower confining clay unit (6) and the uplifted fault zone are also shown. Vertical scale exaggerated by a factor of 10. Locations of the Wente and Davey agricultural wells and the Treatment facility ''B'' (TFB) extraction well are also shown. Initial source location used in transport experiments shown in green. In the electronic version of this paper, two animated sequences are available to help visualize the hydrostratigraphic units and heterogeneous layers more clearly (see ''Special section on Visualization'' on the journal's homepage at **http://www.elsevier.nl/locate/advwatres** or **http:www.elsevier.com/locate/advwatres**).

smaller engineering workstations. It has been optimized for repeated large-scale flow simulations by incorporating a concise, hierarchical and grid-independent representation of the hydrostratigraphic flow units, direct generation of the stochastic property fields via a parallel Turning Bands technique, and an efficient solution of the discretized equations using a multigrid preconditioned conjugate gradient (MGCG) technique.[2]

An efficient, Lagrangian random-walk particle grid model[26,27,29] was used to simulate contaminant migration, dispersion and reaction processes, as embodied in eqn (3). Solutions here were found on single-processor unix workstations. In all simulations, a particle resolution of 3000 particles/kg was used to represent the contaminant mass (dissolved or dissolved + sorbed) in groundwater.

4 FLOW SIMULATIONS

Altogether, five distinct random realizations of the formation properties were considered, along with a sixth in which the individual layer properties were held constant (Table 1). These runs were not meant to support an exhaustive Monte Carlo simulation process, but, rather, to illustrate and gauge some of the basic process variabilities that may occur from one realization to the next.

Within each realization, two types of flow problems were considered. The ''ambient case'' simulation involved finding the steady-state head field in the local subdomain subject to specified hydrostatic head conditions on the perimeter of the domain and no-flow conditions on the top and bottom. The boundary head conditions were interpolated from the measured values shown in Figs 1 and 2. Because these observations were made during the operation of two agricultural wells that lie within the domain, the so-called Wente and Davey wells (Figs 4, 3, and 7) were added to the ambient case simulation. Although these wells go well below the bottom of our domain (into additional permeable zones), only the portions of their screened intervals above the Unit 6 clay layer (132.5 ft in units 3b–5 and 17.5 ft in Unit 5, respectively) were used. As an approximation, the total pumping rate specified was divided evenly among the nodes intersecting the well screen. For both wells, Q_w was set approximately to 9500 ft^3/day.

The ''extraction case'' simulation involved the addition of a remedial extraction well in the area of the currently operating Treatment Facility B (Figs 4, 3, and 7), with all other factors unchanged. The ''TFB'' well was screened over a 12.5 ft interval in Unit 3a near the top of the saturated zone (specifically centered at an elevation of 475 ft), and was pumped at a rate of $Q_w = 5000$ ft^3/day to approximate the current operation. (The real facility is composed of several wells; in addition, several other facilities are being used that are not a part of this simulation, as reviewed in Ref.[28].) All other specifications, including the boundary conditions, remained unchanged from the ambient case.

4.1 Results

In Fig. 8, head profiles from near the top of the domain are shown for the first three realizations of the formation properties. Figures for the ambient and extraction cases are

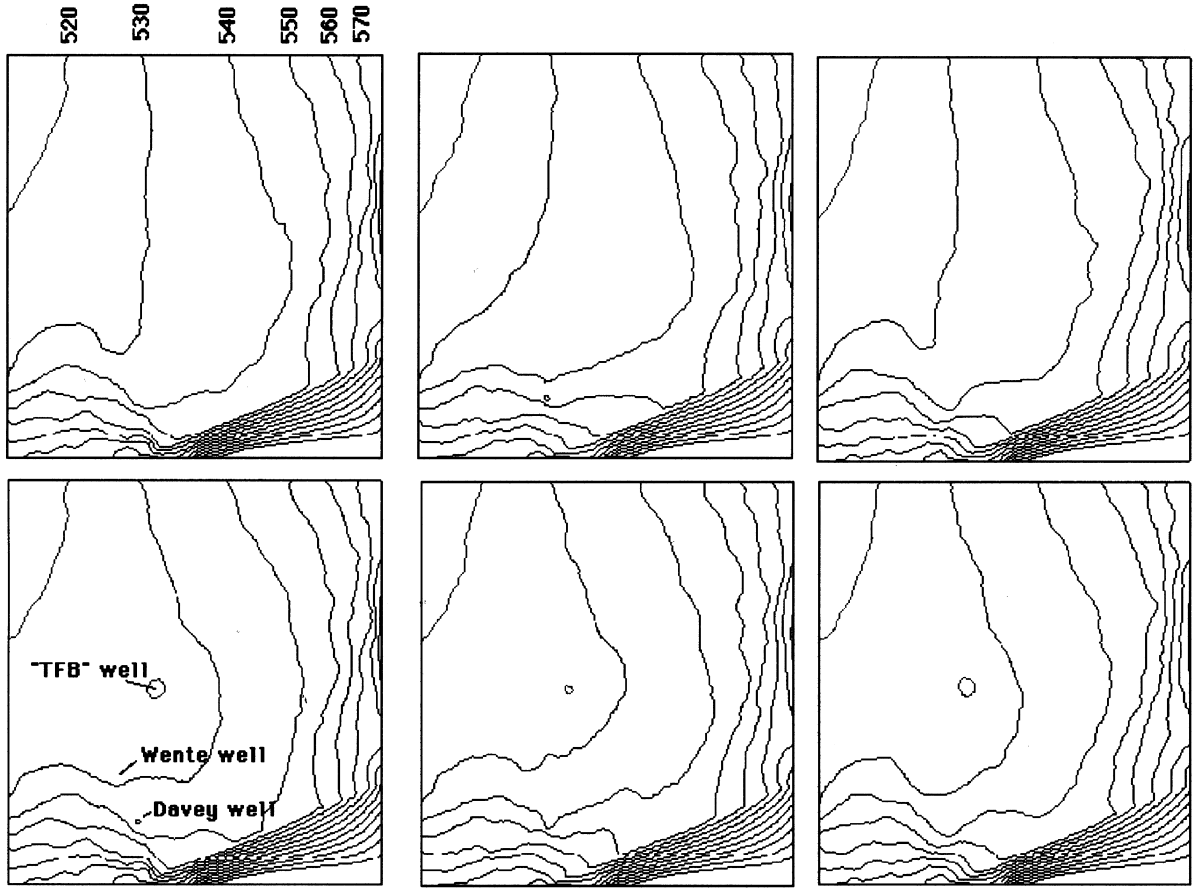

Fig. 8. Head profiles near the top of the domain from three realizations: top row, ambient case; bottom row, remedial case. The upper left contour corresponds to 520 ft; the contours rise to the east and southeast at 10 ft intervals; compare with Fig. 4.

shown on the top and bottom, respectively. The sharp gradient near the southeast corner of the domain correctly represents the influence of the uplifted fault zone. The hydraulic gradients directly beneath LLNL, just to the east of the TFB well, are quite flat and generally agree with observations on the order of 0.0015–0.003. In a broad sense, the different realizations give rise to similar profiles, perhaps partly as a result of the fixed features and boundary conditions used in each simulation. Yet, there are a number of clear and distinct differences. In the first and third run, for example, the impacts of the Wente and Davey wells near the water table correspond well to the measured effects seen in Figs 1 and 2. In the second run, their impacts are more subtly represented, having been reduced by lower permeability materials that were generated near and above the screens of the wells. Because the property realizations were not conditioned to measured data or other observations, neither conditions adjacent to the wells nor those between the well and the water table were necessarily constrained to be permeable.

In Fig. 9, the two head profiles from the first realization are compared to those in the sixth realization in which the geometric-mean hydraulic conductivities (K_{Gj}) were specified as constant scalars in each hydrostratigraphic unit (Table 1 and Fig. 3). Here we see smoother contours following a slightly distorted orientation, implying, possibly, a slightly different capture zone. The most significant effect is that the influence of the pumping wells is much more pronounced near the top of the domain. The geologic structure specified in the heterogeneous case clearly provides a degree of hydraulic insulation.

5 TRANSPORT SIMULATIONS

A series of chemical transport simulations were conducted in the flow fields described above. Pulses of approximately 20 and 36 kg of dissolved tracer and reactive compounds, respectively, were introduced into the groundwater and allowed to migrate under the ambient flow conditions of each realization. The pulse was not meant to represent any particular portion of the contamination at the site, but, rather, to serve in a more hypothetical fashion to examine effective displacement and dispersion processes, as well as being a test case to see how well the TFB well captures this mass.

In all cases, the initial mass was uniformly distributed in a $500 \times 500 \times 5$ ft^3 volume of soil, located roughly 3200 ft to the east–northeast of the TFB well and about 10 ft below the water table (Fig. 3). This initialization volume lies within

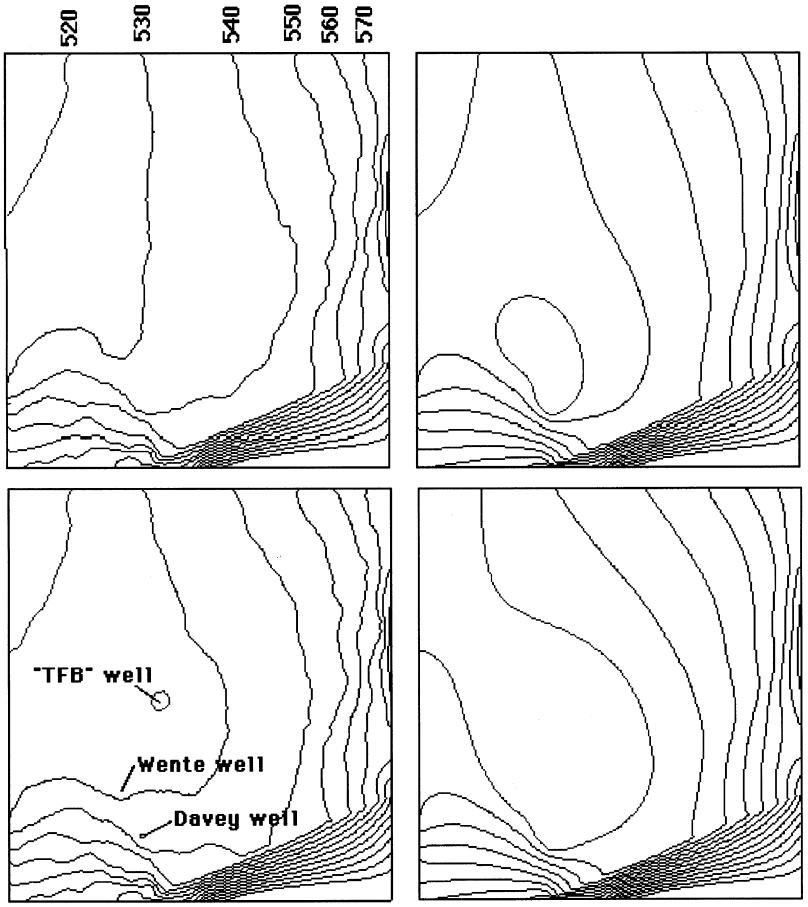

Fig. 9. Head profiles near the top of the domain from the first heterogeneous problem (left) and the uniform problem (right): top row, ambient case; bottom row, remedial case. The upper left contour corresponds to 520 ft; the contours rise to the east and southeast at 10 ft intervals; compare with Fig. 4.

hydrostratigraphic Unit 2 (Table 1) and is centered at an elevation of 528 ft, roughly 45 ft above the screen of the TFB well. For both the tracer and reactive (PCE) compounds, this led to approximate initial aqueous concentrations of 1.89 mg/l, assuming a porosity of 0.3. Given the desired particle resolution of 3000 particles/kg, roughly 60 000 and 72 000 particles were used in each simulation.

It is important to note that the initialization process did not distribute the solute mass in any preferential fashion with respect to the permeability distribution in the initialization area. It was as though the mass was directly introduced through a well or leaky container at this location, or dissolved from a DNAPL that has sunk into or enveloped this zone. If, however, the initial zone of contamination was considered to have originated via historical migration from a disposal point on the ground or water table surface, then the mass would more likely be found inside regions of higher permeability, to the extent that they exist. In this sense, mass should be preferentially distributed into the more permeable parts of the initialization area, or, alternatively, permeabilities generated *a posteriori* in this area should be conditioned towards higher values.

5.1 Results

After initialization, the tracer and reactive compounds were allowed to migrate for 15 000 days (41 years) under ambient flow conditions. The vertically averaged distribution of the nonreactive tracer mass in each realization is shown in Fig. 10a. Clearly, the plumes move relatively slowly because of the low hydraulic gradients in this area. In addition, the plumes show minor and distinct profile differences arising from local variations in each velocity field. In particular, the plume of simulation 4 shows a marked lack of displacement and spreading, because the initial plume location in this realization was situated in a zone of low permeability.

After 15 000 days, migration was allowed to continue under extraction flow conditions. In this sense, the images in Fig. 10a would correspond to the contaminant distribution at a time of ''discovery'', say 41 years or so after their introduction into the groundwater. Fig. 10b shows the distribution of the same tracer contaminants after another 15 000 days has passed under the extraction scenario. At this stage, mass is clearly moving toward the TFB well, although not much of it seems to have been captured (recall that the location of the well was not really chosen

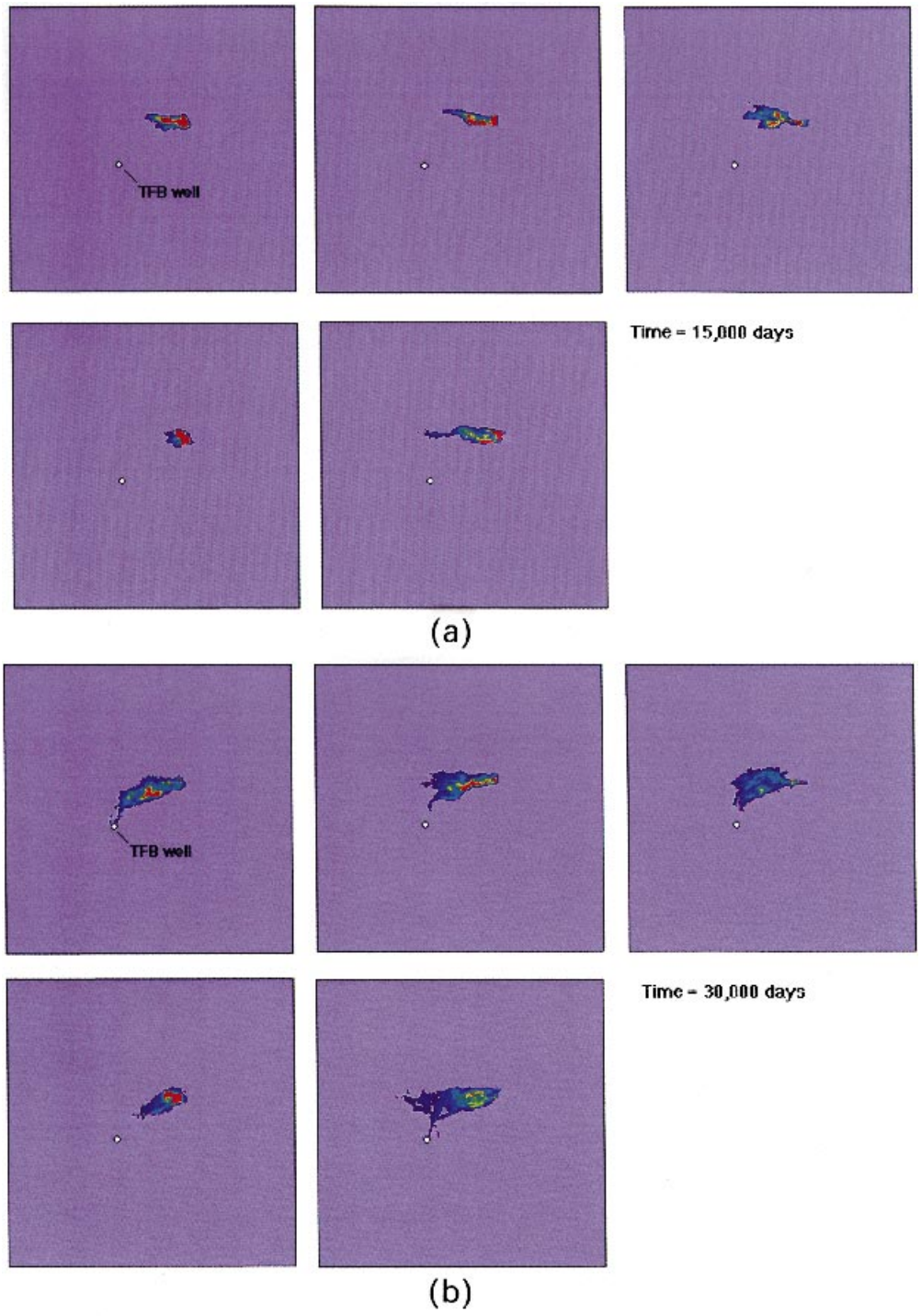

Fig. 10. Vertically averaged tracer concentration from five realizations after (a) 15 000 days (41 years); (b) 30 000 days (82 years). Recall that extraction (TFB) well was turned on after 15 000 days. In the electronic version of this paper, a series of animated montages are available to help visualize the two-dimensional, vertically averaged tracer migration in a composite of all realizations more clearly (see ''Special section on Visualization'' on the journal's homepage at **http://www.elsevier.nl/locate/advwatres** or **http:www.elsevier.com/locate/advwatres**).

to optimize the extraction of the contaminants as they appear in Fig. 10a). Notice that the overall mobility of the plume in simulation 4 is still significantly reduced. However, because of the proximity of Unit 1b (Fig. 3), some of the mass has moved into this unit and moves faster.

Fig. 11 shows the extraction history of both the tracer and reacting compounds at the TFB well over time. In the left column, the vertically averaged tracer distribution for the first realization at 30 000 days (82 years) is shown, along with the mass recovery for the tracer (solid lines) and sorbing compound (dotted lines) for each of the five realizations. Clearly, there is a fair degree of variability in the results, perhaps more than might be interpreted from the integrated profiles at 15 000 and 30 000 days. Over a 250 year period,

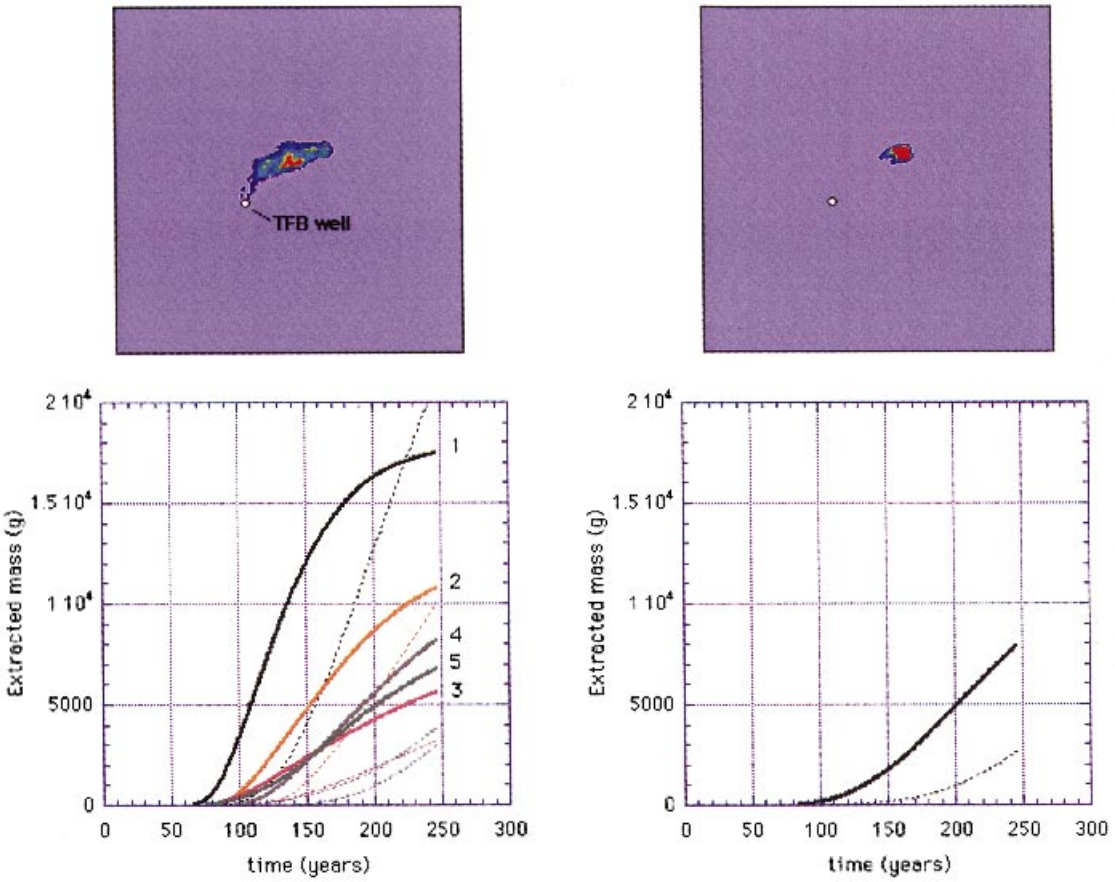

Fig. 11. Stochastic and deterministic extraction results. Left side: vertically averaged tracer concentration at 30 000 days for the first heterogeneous problem and extraction history for both compounds in all five heterogeneous realizations (solid line = tracer, dotted line = reactive compound). Right side: vertically averaged tracer concentration at 30 000 days for the deterministic problem (constant layer K_G values) and the associated extraction history.

most of the 20 kg of tracer mass was recovered in one simulation, while barely one-third of it was recovered in another. An even wider gap is evident with the sorbing (PCE) compound, even though its recovery has not quite reached any limiting value(s) because of retarded migration rates. The variability in recovery reflects the uncertainty that heterogeneity introduces and the overall impact heterogeneity has on the integrated migration rates between the source area and the well. Some of this variability is also due to the way in which the initial condition was established. If the initial mass were apportioned (or conditioned) to regions of higher permeability, then the variability between these results would likely be reduced.

In the second column of Fig. 11, a similar set of results is shown for the sixth medium realization in which the geometric mean hydraulic conductivities were specified uniformly as constants within each unit. Compared with the previous results, the tracer plume shows a smaller overall mean displacement, and, aside from some mass crossing into faster flows in Unit 1b, virtually no macrodispersion associated with heterogeneity is evident. As observed over a 300 year period, complete tracer recovery (20 kg) was not obtained because some of the mass appears to have moved outside the capture zone of the well.

6 ASSESSMENT OF EFFECTIVE BEHAVIOR

The differences observed between the uniform and nonuniform simulations arise for two reasons: first, the geometric mean conductivities used as the ''constant'' layer values in the sixth realization do not adequately represent the effective behavior produced in the heterogeneous problems. Secondly, the macrodispersive effect produced by the heterogeneity in the first five realizations is not truly represented in the sixth one. To assess this situation further, the tracer transport problems were all run again under ambient conditions only, for a period of 120 000 days (329 years), or until all of the mass exited the domain. This produced a set of ''ambient-only'' results. In this way, the displacement and macrodispersive behavior of the plumes could be measured in the absence of treatment well influences.

6.1 Mean tracer plume displacement and effective horizontal conductivity

In Fig. 12a, the path-length displacement, $s(t)$, of the center of mass of each tracer plume in the first five ambient-only realizations is shown. These were computed using the procedure of Tompson and Gelhar.[26,27] All are rather

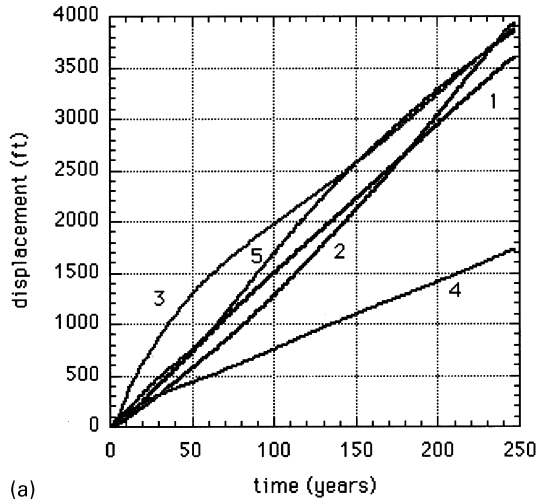

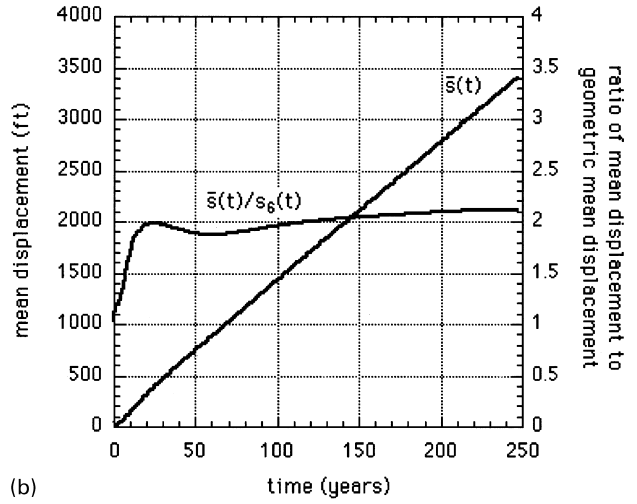

Fig. 12. Estimates of the path-length displacement as a function of time, $s_i(t)$ in the ambient-only simulations, (a) for the five nonuniform realizations ($i = 1$–5), and (b) for the sixth uniform realization ($i = 6$). In (b), the average of the five nonuniform results ($\bar{s}(t)$) is also shown, as well as the ratio $\bar{s}(t)/s_6(t)$.

similar, except for the fourth realization which shows a distinctly slower migration rate. This resulted from the mass initialization factors associated with this problem, as discussed previously.

The average of these five displacement curves is shown in Fig. 12b. The ratio of the average displacement to the displacement observed in the sixth (constant property) realization is also shown. Allowing for initialization effects, it is clear that the average rate of migration in the constant property problem is slower by a factor of 1.9–2.1. This was determined by using the displacement ratio as an approximate speed ratio. Assuming that hydraulic gradients are roughly similar in all of these problems, this factor may be a good approximation of the ratio of the apparent, or ''effective'', horizontal hydraulic conductivity ($\hat{K}_h$) to the geometric mean conductivity (K_G) within the hydrostratigraphic layers through which the tracer passed.

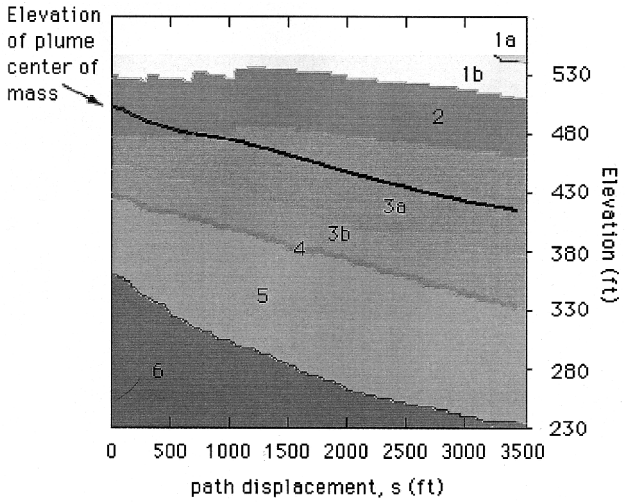

Fig. 13. Elevation of the plume center of mass for the first ambient only simulation. Results are plotted as a function of displacement and hydrostratigraphic unit.

This ratio may also be estimated for specific hydrostratigraphic layers by employing theoretical results from the stochastic models of Dagan[8] (equations 3.4.17–18), Gelhar[12] (equation 4.1.62 and Fig. 4.8) or Neuman and Orr[16] (equations 37–39). In the case of an unbounded, stratified medium characterized by a stationary correlation structure (eqn (6)) with $\lambda_1 = \lambda_2$ and $e = \lambda_3/\lambda_1$, these results generally indicate that

$$\hat{K}_h/K_G \approx 1 + \frac{\sigma_f^2}{2}(1 - \mathcal{F}(e)) \tag{8}$$

where $\mathcal{F}(e)$ is a complicated function of the degree of stratification. Using Dagan's[8] equations (3.4.17–18), we have estimated $\hat{K}_h/K_G$ values for each hydrostratigraphic layer, as shown in Table 1. Equivalent values were found from the other cited results.

These results indicate that a tracer plume moving in a heterogeneous version of Unit 2 should be moving approximately 1.9 times faster than an equivalent plume in a uniform version characterized by the geometric mean conductivity, assuming equal hydraulic gradients. Similarly, a plume moving in a heterogeneous version of Unit 3a should be moving 3.45 times faster than an equivalent plume in a similar uniform version. The results of Fig. 12b reflect the behavior of plumes that could be moving in several units at different times, or simultaneously. Fig. 13 tracks the elevation of the center of mass of the tracer plume for the first ''ambient only'' simulation, and confirms that the plume moves from Unit 2 to Unit 3a over the course of the simulation, paralleling the slight dip in the bedding. This same course was observed in all other simulations as well. In all cases, portions of the plumes span Units 2, 3a and 3b near the end of the simulation. Hence, it is reasonable to assume the speed ratio estimated in Fig. 12b (1.9–2.1) reflects some average of the effective conductivity ratios predicted for Units 2 and 3a (1.9 and 3.4).

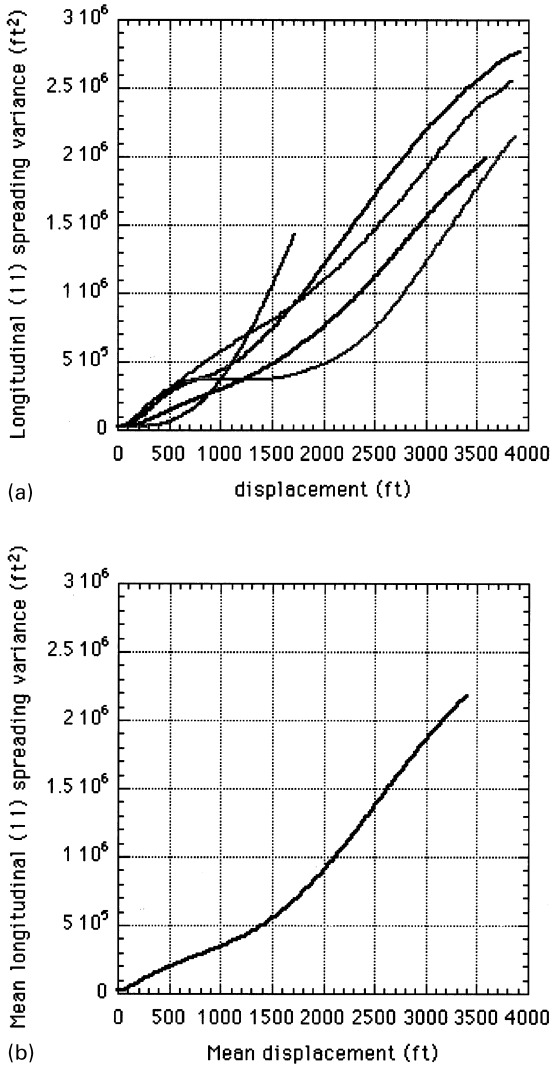

Fig. 14. Evolution of the longitudinal spreading variance, Σ_{11}^2 as a function of path-displacement, s, (a) for each of the nonuniform ambient-only realizations, and (b) as averaged over all five realizations.

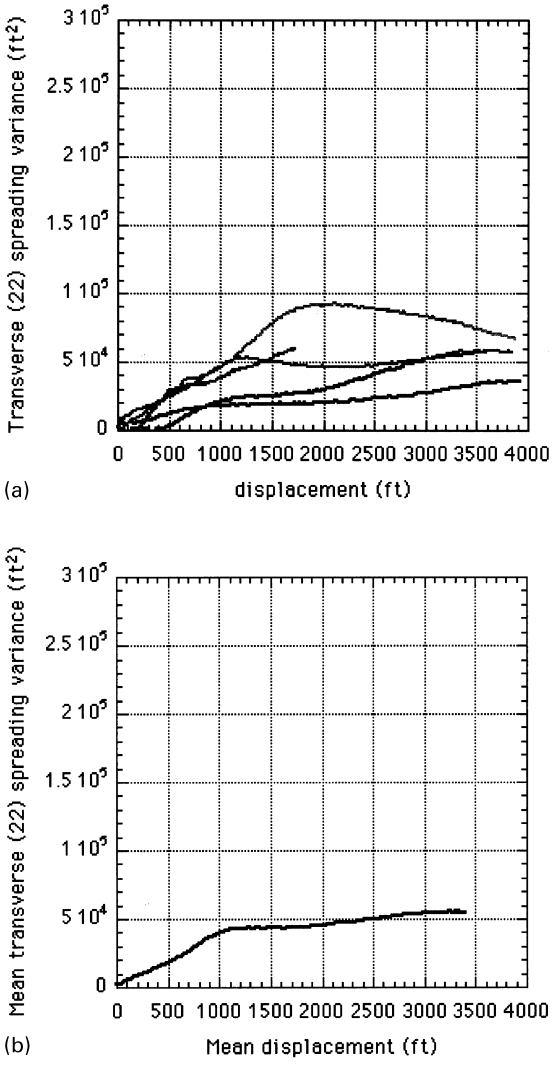

Fig. 15. Evolution of the transverse spreading variance, Σ_{22}^2 as a function of path-displacement, s, (a) for each of the nonuniform ambient-only realizations, and (b) as averaged over all five realizations.

Although not included in Table 1, it is interesting to note that better agreements (in terms of apparent effective hydraulic conductivities) were found with expressions of the form given in eqn (8), as opposed to their exponential generalizations (equation (4.1.65) in Ref.[12] or equation (40) in Ref.[16]). This agreement occurred here and in several other unpublished comparisons despite the fact that the corresponding vertical effective conductivities, predicted by results similar to eqn (8), can often be negative.

The results in Table 1 indicate the effective horizontal hydraulic conductivities in the local subdomain range from 3.8 to 14.0 ft/day. Surprisingly, these tend to bracket the 10.0 ft/day value used in the central region of the calibrated two-dimensional regional model of the LLNL site described in Ref.[28], despite the fact that the influence of the lower permeability materials was not incorporated in the current analyses.

6.2 Tracer plume spreading and macrodispersive behavior

In Figs 14–16, parts a, the principal components of the tracer plume spreading variance tensor, $\Sigma_{ii}^2(s)$ (no sum), are plotted as a function of path-length displacement, $s(t)$, for the first five ambient-only realizations. These components can be used to gauge the size of a plume in a given direction and determine its rate of growth (or spreading) as a function of mean displacement. They may be used to assess the nature of macrodispersion, and in particular, to determine whether constant macrodispersivity components can be identified and measured. As above, these components were computed using the procedure of Tompson and Gelhar.[26,27]

The predominant axis of spreading occurs in the longitudinal direction (Fig. 14a), roughly parallel with the mean direction of plume displacement. The spreading rate in the (approximately) horizontal bedding plane

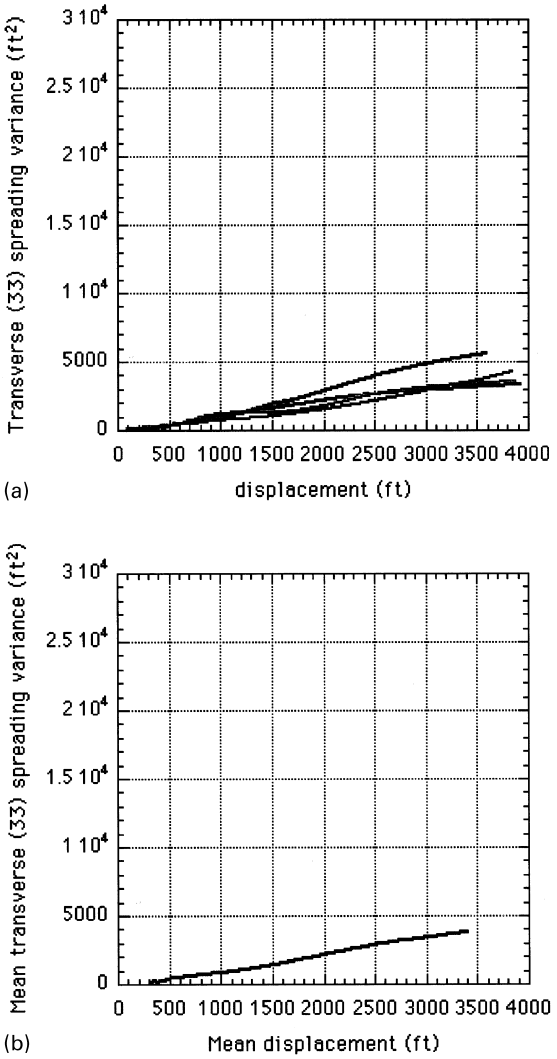

Fig. 16. Evolution of the transverse spreading variance, Σ_{33}^2 as a function of path-displacement, s, (a) for each of the nonuniform ambient-only realizations, and (b) as averaged over all five realizations.

perpendicular to the longitudinal axis (Fig. 15a) is an order of magnitude smaller, while that in the vertical direction, perpendicular to the bedding plane (Fig. 16a), is still another order of magnitude smaller.

Each set of curves shows a marked degree of variability from one realization to the next. This reflects the contorted stretching and squeezing each plume undergoes during displacement.[26] Comparison of Fig. 14a and b shows that when one plume is comparatively longer in the longitudinal direction than the rest, it is generally thinner in the transverse horizontal direction as well.

In Fig. 14a, the longitudinal spread or variance observed in most realizations appears to increase at one rate for the first 1200 ft of displacement, and then at a much larger rate thereafter. This is better seen in Fig. 14b in which the average value from the five realizations is plotted. These different apparent rates may be due to a developmental process associated with generalized plume expansion (e.g. Dagan,[8] Fig. 4.6.1; Gelhar,[12] p. 235), variabilities associated with the plume moving through different hydrostratigraphic layers (e.g. Fig. 13), or a combination of both.

In general, the accelerated growth or spreading induced by the heterogeneity may be described as an effective or macroscopic dispersion process characterized by a tensor $\mathbf{D}_m$ whose principal (or diagonalized) form looks like[8,12,26]

$$\mathbf{D}_m(s) \approx \begin{bmatrix} A_{11}(s)+\alpha_L & 0 & 0 \\ 0 & A_{22}(s)+\alpha_T & 0 \\ 0 & 0 & A_{33}(s)+\alpha_T \end{bmatrix} \cdot \frac{ds}{dt} \tag{9}$$

The principal longitudinal axis of $\mathbf{D}_m$ is generally considered to be aligned in the direction of mean plume displacement, although some departures from this have been discussed in cases where the mean hydraulic gradient is not aligned with the horizontal bedding plane.[12] Notice the explicit dependence of $\mathbf{D}_m$ on the mean displacement $s(t)$ and displacement rate ds/dt. The role of molecular diffusion has been ignored. The apparent principal macrodispersivity components, A_{ii} (no sum), may be estimated from the averaged plots in Figs 14–16, parts b, by[26]

$$A_{11}(s)+\alpha_L \approx \frac{1}{2}\cdot\frac{d\Sigma_{11}^2}{ds} \tag{10}$$

$$A_{22}(s)+\alpha_T \approx \frac{1}{2}\cdot\frac{d\Sigma_{22}^2}{ds}$$

$$A_{33}(s)+\alpha_T \approx \frac{1}{2}\cdot\frac{d\Sigma_{33}^2}{ds}$$

Estimates of A_{ii} (no sum) measured from these plots are shown in Table 2 for two different displacement ranges. Although the range $0 < s(t) < 1200$ ft may be construed as a ''developmental'' region, it does correspond to a good part of the displacement and growth of the plume observed during the first 30 000 days of the simulations shown in

Table 2. Estimated ''total'' (principal component) dispersivities for the plumes run in the heterogeneous ''ambient-only'' simulations, as based on the measured spreading rates shown in Figs 14–16. The range $s > 2000$ ft may be considered ''asymptotic''. Recall $\alpha_L = 1.0$ ft and $\alpha_T = 0.1$ ft

Displacement range (ft)	$A_{11} + \alpha_L$ (ft)	$A_{22} + \alpha_T$ (ft)	$A_{33} + \alpha_T$ (ft)
$0 < s(t) < 1200$	165	19	0.5
$2000 < s(t) < 3400$	473	3.8	0.6

Table 3. Effective asymptotic macrodispersivities for each hydrostratigraphic unit using the results of Dagan[8] (equations 3.4.17–18), Gelhar[12] (equation 5.2.18) and the data in Table 1. These results are based upon the assumption that the hydraulic gradient lies approximately in the plane of bedding. In this case, both Dagan's and Gelhar's results suggest that $A_{22}(\infty) = A_{33}(\infty) = 0$. Rajaram and Gelhar's reduction factors can be used to estimate modified values $A^*_{11}(\infty) = A_{11}(\infty)\cdot f$

Unit, j	$A_{11}(\infty)$ (ft) (eqn 11)) $\gamma = 1$ (Dagan)	$\gamma = \hat{K}_h/K_G$ (Gelhar)	Correction factors, f, leading to $A^*_{11}(\infty) = A_{11}(\infty)\cdot f$ equation 41 in Ref. 19	equation 42 in Ref. 19
1a	882	95	0.85	0.85
1b	512	107	0.85	0.85
2	392	107	0.85	0.85
3a	1058	89	0.85	0.85
3b	1058	89	0.85	0.85
4	450	108	0.85	0.85
5	800	98	0.85	0.85
6 (clay)	392	107	0.85	0.85
Fault zone	0.0	0.0	0	0

Fig. 10. For $s(t) > 2000$ ft, the slopes of the spreading curves are generally constant and the components might be considered to have reached asymptotic values. Note that $A_{22}(\infty)$ is much smaller that its preasymptotic value and that the magnitudes of $A_{33}(\infty)$ and α_T are somewhat comparable. Note also that the average value of Σ^2_{33} at $s =$ 3000 ft is 3500 ft^2; this corresponds to a characteristic vertical plume thickness of $\pm\,\Sigma_{33} = 60$ ft about the center of mass, confirming that the plumes eventually do span Units 2, 3a and 3b in the simulations (Fig. 13).

From a theoretical perspective, both Dagan[8] (equations 4.6.21) and Gelhar[12] (equation 5.2.18) offer predictions of the asymptotic values of the macrodispersion coefficients as a function of the statistical medium characteristics (Table 1) and the orientation of the mean background hydraulic gradient. They have been developed for unbounded, statistically stationary media that are more idealized than the current layered system. If the mean hydraulic gradient can be considered to be aligned with the plane of bedding and $\lambda_1 = \lambda_2 = \lambda_h$, then the appropriate results are

$$A_{11}(\infty) \approx \frac{\sigma_f^2 \lambda_h}{\gamma^2} \tag{11}$$

$$A_{22}(\infty) \approx 0$$

$$A_{33}(\infty) \approx 0$$

The γ term in eqn (11) is defined by Gelhar[12] to be $\gamma \approx \hat{K}_h/K_G$. Dagan[8] and others consider this term unnecessary such that $\gamma = 1$. More recently, Rajaram and Gelhar[19] have suggested the values of $A_{11}(\infty)$ in eqn (11) may overestimate the actual spreading behavior, and have proposed modified values of the form

$$A^*_{11}(\infty) \approx A_{11}(\infty)\cdot f \tag{12}$$

where the reduction factor $f < 1$ is dependent on the correlation structure and the asymptotic values of the spreading variance components Σ^2_{22} and Σ^2_{22}.

Values of $A_{11}(\infty)$ computed from eqn (11) and the data in Table 1 are shown in Table 3. Estimates of Rajaram and Gelhar's[19] reduction terms based upon their equations (41) and (42) are also shown. These results are based upon asymptotic estimates of Σ_{22} and Σ_{33} inferred from Figs 15 and 16, parts b (equal to 224 and 60 ft, respectively) and are developed for bounding situations where $\Sigma_{33} \gg \lambda_3$ and $\Sigma_{22} \gg \lambda_2$ or $\Sigma_{33} \gg \lambda_3$ and $\Sigma_{22} < \lambda_2$, respectively.

If, as above, the tracer plumes are regarded to migrate principally in hydrostratigraphic Units 2 and 3a (Fig. 13), then the value $A_{11}(\infty) = 473$ ft measured from the simulations compares more favorably with the range of Dagan's results predicted for these units ($A_{11}(\infty) \approx$ 392–1058 ft), especially when modified by either of Rajaram and Gelhar's[19] reduction factors (to yield $A^*_{11}(\infty) \approx$ 333–899 ft). Nevertheless, a more exacting comparison to theory may be more difficult because of the plumes' trajectory through the various hydrostratigraphic units.

The extremely small measured values of $A_{22}(\infty)$ and $A_{33}(\infty)$ shown in Table 2 seem approximately consistent with the predicted zero values. In addition, the apparent growth and eventual decline of $A_{22}(s)$ towards $A_{22}(\infty)$ seems consistent with predictions of preasymptotic behavior as well, although some of the observations could have been produced by plume transitions between different layers and offsets between the slight dip structure of the layers and the orientation of the mean hydraulic gradient. Indeed, Gelhar,[12] (Fig. 5.14) suggests that nonzero values of $A_{22}(\infty)$ and $A_{33}(\infty)$ may be obtained if the mean gradient is not perfectly aligned in the plane of bedding.

6.3 One last simulation

In order to assess how well the behavior in the heterogeneous problems could be reproduced in a mean sense using effective parameters, we have rerun the previous deterministic flow problem using effective horizontal conductivities shown in Table 1 in place of the geometric mean values specified previously.

Following this, a transport simulation was conducted with

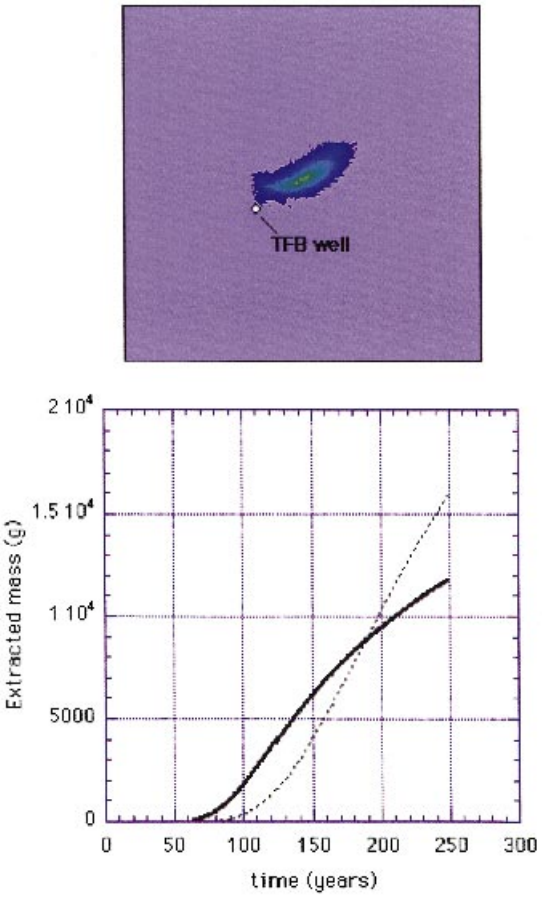

Fig. 17. Deterministic extraction results. Vertically averaged tracer concentration at 30 000 days for the deterministic problem (constant layer $\hat{K}_h$ values) and the associated extraction history for both compounds (solid line = tracer, dotted line = reactive compound).

constant macrodispersivities that are approximately consistent with the values measured in the heterogeneous simulations. Specifically, we solved eqn (3), where the diagonalized form of **D** is given by eqn (9), and used constant values of $A_{11} \approx 165$ ft, $A_{22} \approx 19$ ft and $A_{33} \approx 0.5$ ft (Table 2). These values were deemed appropriate for plume displacements less than 1200 ft, and were not modified or adjusted to match characteristics of each hydrostratigraphic layer (alternatively, one could attempt to estimate approximate values from the preasymptotic regime of equation (4.6.14,15) of Dagan[8]).

This simulation required a slight modification of the model to treat three principal dispersivity values instead of two. It was felt that larger values consistent with the apparent or predicted asymptotic values shown in Table 2 or Table 3 would lead to overdispersed plumes in the near field and poor capture results.

Fig. 17 shows the tracer distribution at 30 000 days and the extraction history of the tracer and reactive compounds. Clearly, the areal shape and center of mass of the plume more closely approximate those created in the nonuniform flow fields, even though the plume trajectory appears somewhat different. The recovery curve, albeit incomplete, seems fairly well bracketed by the heterogeneous results. This approach necessarily approximates developmental dispersion behavior with inferred constant preasymptotic dispersion coefficients, and did not incorporate anisotropy in the conductivity specification. ''Nonstationary'' effects induced by the well or boundary effects were not addressed.[16] In addition, no sense of the recovery uncertainty induced by fundamental data uncertainties (Fig. 11a) can be discerned from this result.

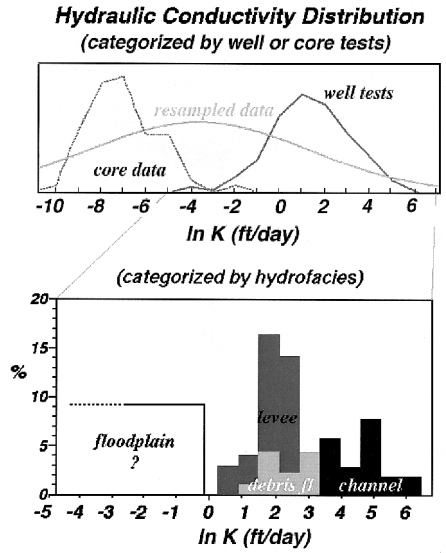

Fig. 18. Below: distribution of lithologic materials sampled by the wells tested at the LLNL site, sorted by the measured conductivity (after Carle[5]). Above: hypothethical resampled Gaussian ln K distribution superposed on the well and core test data (as obtained by matching the mean and variance of the properties assigned to the lithological facies and weighted by lithological abundance).

7 ADDITIONAL OBSERVATIONS AND CONCLUSIONS

In this paper, we have reported on a series of detailed simulations to test the applicability and utility of stochastic models of flow and transport in porous media in the context of a real field system. The process has led to a number of pertinent insights relating to

- the intrinsic viability of stochastic models, both in terms of their applicability to real field systems as well as their theoretical accuracy;
- a need for better and unbiased methods to delineate the spatial distribution and structure of geologic materials and hydraulic properties in field systems; and
- the importance of large-scale simulation as a tool to provide valuable insights on small-scale mass transport processes in highly variable media.

7.1 Model viability

Understandably, the configuration of the application site has presented some apparent nonidealities with respect to the basic stochastic modeling framework. As formulated, the problem was posed in a bounded domain, based upon a multi-layer random-field conceptualization, and made more complicated through the inclusion of several pumping wells. These issues created a nonstationary environment that is, strictly speaking, beyond the realm of applicability of the more traditional stochastic theories. Moreover, because the $\ln K$ variances (σ_f^2) used in the layers range between 2 and 5.3, they are seemingly out of the range of the low-variance assumptions typically employed.

Nevertheless, the observed rates of plume displacement in the simulations suggest that the effective horizontal hydraulic conductivities of the different layers are in approximate agreement with predictions based upon eqn (8), at least as they apply to Units 1b and 2. Estimates of the asymptotic tracer macrodispersivity based upon Dagan's model,[8] as corrected by Gelhar and Rajaram's[19] results, appear to bracket the overall value observed in the long-term ambient-case model simulations. Use of smaller, pre-asymptotic macrodispersivities in an effective medium extraction-case simulation provided a set of contaminant recovery curves that are clearly enveloped by those found in the high-resolution simulations conducted earlier.

7.2 On the need for improved geologic characterization

Although the simulations suggest a certain robustness in many of the stochastic results, it appears that biases and limitations in the original hydraulic data may have reduced the applicability of the Gaussian representations and clouded the practical utility of the simulations and effective behavior based upon them. The disparity in scale and biases that are evident in the core and well test data (Fig. 5a) suggest that some blending of the data sets would be desirable. Moreover, the representation of geologic structure and spatial correlation in the system needs to be improved.

On the one hand, this might be achieved by performing additional well tests in a wider range of media that includes lower permeability materials and more closely-spaced data locations in horizontal directions. However, the costs would be prohibitive and the success of measuring the permeability of tight clays with traditional testing procedures would be questionable at best. On the other hand, a greater focus on testing core-scale samples might lead to better distributional measurements of permeability, but may again suffer from excessive costs and experimental constraints.

Evolving trends in geologic characterization seem to be focused on the greater use of noninvasive geophysical characterization methods[20,9,7,13] and more realistic geostatistical or depositional modeling techniques that respect and incorporate a greater amount of existing geologic information.[14,10,15,18,21,31,6,11] Geostatistical indicator techniques, for example, are based upon modeling the structure and distribution of hydraulically distinct lithologic materials as opposed to hydraulic conductivity properties themselves. Distributional information is readily available from borehole data, while structural information can be more easily inferred from principles of geologic deposition, as well as trench and cross-borehole observations.

In a new application at LLNL, Carle and others[5,11] have shown that the hydraulic tests largely sample the channel, debris flow and levee materials in the alluvium, but none of the floodplain materials (Fig. 18). Interestingly, the floodplain materials alone comprise over 50% of the alluvial volume, and are most likely representative of the materials tested in the cores. The average hydraulic conductivity for the floodplain, levee, debris flow and channel materials has been estimated to be 1.4×10^{-4}, 0.57, 1.42 and 17.0 ft/day, respectively.[5] When weighted by an estimate of the fractional abundance of these materials in the aquifer, the geometric mean conductivity is estimated as 0.03 ft/day, while the apparent $\ln K$ variance (σ_f^2) is over 24!

If a Gaussian $\ln K$ distribution with these parameters is superposed on the well and core test data, a resampled curve is obtained that effectively spans the entire data set (Fig. 18). Although the real facies distribution is not likely to be Gaussian, this suggests that a more unified and unbiased picture of the permeability distribution is being achieved in this process.

7.3 High performance computing

The structure and distribution of geologic materials produced in newer geologic modeling approaches are generally more flexible and geologically realistic than those produced by traditional random-field models. As a result, these models offer new opportunities for investigating fine-scale mass transport issues and interpreting large-scale effective flow behavior, both at LLNL, and in other, geologically complex systems.

The lack of theoretical models describing effective flow and macrodispersion behavior in more general geologic representations emphasizes the fact that large-scale simulation of the sort used here can be of much greater importance and utility in these endeavors. This point becomes much more relevant when the flow, transport and transformation processes become increasingly complicated, coupled, mathematically nonlinear and sensitive to small-scale material variabilities.

Thus, it would appear that flow and mass transport simulations in complex media will become increasingly important in the future as related to the following areas:

- complicated remedial technology and waste management topics involving multiphase flow or microbiological, chemical or thermally enhanced transport and transformation processes;
- scientific justification of dilution and other natural attenuation phenomena in support of negotiated

closures of contamination sites and improved groundwater driven risk assessment studies;
- broader groundwater quality issues associated with non-point source pollution, agricultural inputs and aquifer recharge practices; and
- large-scale aquifer, surface water and conjunctive use management policies.

7.4 Animations and electronic copy

This paper can be viewed electronically at the journal's homepage at **http://www.elsevier.nl/locate/advwatres** or **http://www.elsevier.com/locate/advwatres** (see ''Special section on Visualization''). The electronic version includes a number of animated sequences associated with Figs. 3, 7, 10 and 11.

ACKNOWLEDGEMENTS

This work was conducted under the auspices of the U.S. Department of Energy by Lawrence Livermore National Laboratory under contract W-7405-Eng-48. It was supported, in part, by the Strategic Environmental Research and Development Program of the U.S. Department of Defense, through the cooperation of the USAE Waterways Experiment Station, Vicksburg, MS. The contributions of Richard Blake, Steven Carle, Thomas Fogwell, Graham Fogg, Robert Gelinas, Michael Maley and Charles Noyes are gratefully acknowledged.

REFERENCES

1. Ashby, S. F., ParFlow home page: http://www.llnl.gov/CASC/ParFlow/, 1996.
2. Ashby, S. F. and Falgout, R. D. A parallel multigrid preconditioned conjugate gradient algorithm for groundwater flow simulations. *Nuclear Science and Engineering*, 1996, **124**(1), 145–159.
3. Bishop, D., Rice, D., Rogers, L. and Webster-Scholten, C., Comparison of field-based distribution coefficients (K_d's) and retardation factors (R's) to laboratory and other determinations of K_d's. Lawrence Livermore National Laboratory, Livermore, CA (UCRL-AR-105002), 1990.
4. Blake, R. G., Maley, M. P. and Noyes, C. M., Hydrostratigraphic analysis—the key to cost effective ground water cleanup at Lawrence Livermore National Laboratory. Lawrence Livermore National Laboratory, Livermore, CA (UCRL-JC-120614), 1995.
5. Carle, S. F., A transition probability-based approach to geostatistical characterization of hydrostratigraphic architecture. Ph.D. dissertation, University of California, Davis, 1996, 238 pp.
6. Carle, S. F. and Fogg, G. E. Modeling spatial variability with one- and multidimensional Markov chains. *Mathematical Geology*, 1997, **28,** 453–476.
7. Copty, N. and Rubin, Y. A stochastic approach to the characterization of lithofacies from surface seismic and well data. *Water Resources Research*, 1995, **31**(7), 1673–1686.
8. Dagan, G., *Flow and Transport in Porous Formations*. Springer Verlag, Berlin, 1989.
9. Daily, W., Ramirez, A., LaBreque, D. and Nitao, J. Electrical resistivity tomography of vadose zone water movement. *Water Resources Research*, 1992, **28**(5), 1429–1442.
10. Deutsch, C. V. and Journel, A. G., *Geostatistical Software Library and User's Guide*. Oxford University Press, New York, 1992, 340 pp.
11. Fogg, G. E., Noyes, C. D. and Carle, S. F., Geologically-based model of heterogeneous hydraulic conductivity in an alluvial setting. *Hydrogeology J.*, 1998, in press.
12. Gelhar, L. W., *Stochastic Subsurface Hydrology*. Prentice Hall, New York, 1993.
13. Hyndman, D. W. and Gorelick, S. M. Estimating lithologic and transport properties in three-dimensions using seismic and tracer data. The Kesterson aquifer. *Water Resources Research*, 1996, **32**(9), 2659–2670.
14. Journel, A. and Alabert, F., New method for reservoir mapping. *Journal of Petroleum Technology* 1990, **42**(2) 212–218.
15. Jussel, P., Stauffer, F. and Dracos, T. Transport modeling in heterogeneous aquifers, 1. Statistical description and numerical generation of gravel deposits. *Water Resources Research*, 1994, **30**(6), 1803–1817.
16. Neuman, S. P. and Orr, S. Prediction of steady state flow in nonuniform geologic media by conditional moments—exact nonlocal formalism, effective conductivity, and weak approximation. *Water Resources Research*, 1993, **29**(2), 341–364.
17. Painter, S. Evidence for non-Gaussian scaling behavior in heterogeneous sedimentary formations. *Water Resources Research*, 1996, **32**(5), 1183–1195.
18. Poeter, E. P. and McKenna, S. A. Reducing uncertainty associated with groundwater flow and transport predictions. *Ground Water*, 1995, **33**(6), 899–904.
19. Rajaram, H. and Gelhar, L. W. Plume scale dependent dispersion in heterogeneous aquifers, 2. Eulerian analysis and 3-dimensional aquifers. *Water Resources Research*, 1993, **29**(9), 3261–3276.
20. Rubin, Y., Mavko, G. and Harris, J. Mapping permeability in heterogeneous aquifers using hydrologic and seismic data. *Water Resources Research*, 1992, **28**(7), 1809–1816.
21. Scheibe, T. D. and Freyberg, D. L. Use of sedimentological information for geometric simulation of natural porous media structure. *Water Resources Research*, 1995, **31**(12), 3259–3270.
22. Smith, R. W., Schafer, A. L. and Tompson, A. F. B., Theoretical relationships between reactivity and permeability for monomineralic porous media. *Materials Research Society Symposia Proceedings*, Vol. 412. Materials Research Society, Pittsburgh, PA, pp. 693–700.
23. Thorpe, R. K., Isherwood, W. F., Dresen, M. D. and Webster-Sholten, C. P. (Eds), CERCLA Remedial Investigations Report for the LLNL Livermore Site. Lawrence Livermore National Laboratory, Livermore, CA (UCAR-10299), 1990.
24. Tompson, A. F. B., Ababou, R. and Gelhar, L. W. Implementation of the three dimensional turning bands random field generator. *Water Resources Research*, 1989, **25**(10), 2227–2243.
25. Tompson, A. F. B., Flow and transport within the saturated zone beneath LLNL: Modeling considerations for heterogeneous media. Lawrence Livermore National Laboratory, Livermore, CA (UCID-21828), 1990.
26. Tompson, A. F. B. and Gelhar, L. W. Numerical simulation of solute transport in three-dimensional, randomly heterogeneous porous media. *Water Resources Research*, 1990, **26**(10), 2541–2562.
27. Tompson, A. F. B. Numerical simulation of chemical migration in physically and chemically heterogeneous porous media. *Water Resources Research*, 1993, **29**(11), 3709–3726.

28. Tompson, A. F. B., McKereghan, P. F. and Nichols, E.M. (Eds), Preliminary simulation of contaminant migration at the Lawrence Livermore National Laboratory. Lawrence Livermore National Laboratory, Livermore CA (UCRL-ID-115991), 1995.
29. Tompson, A. F. B., Schafer, A. L. and Smith, R. W. Impacts of physical and chemical heterogeneity on co-contaminant transport in a sandy porous medium. *Water Resources Research*, 1996, **32**(4), 801–818.
30. Webb, E. Simulating the three-dimensional distribution of sediment units in braided stream deposits. *Journal of Sedimentary Research*, 1994, **B64**(2), 219–231.
31. Webb, E. and Anderson, M. Simulation of preferential flow in three-dimensional, heterogeneous conductivity fields with realistic internal architecture. *Water Resources Research*, 1996, **32**(3), 533–545.